PAPER

Structure–property relations in hexagonal and monoclinic BiPO$_4$:Eu^{3+} nanoparticles synthesized by polyol-mediated method†

P. Arunkumar, C. Jayajothi, D. Jeyakumar and N. Lakshminarasimhan*

Hexagonal BiPO$_4$·xH$_2$O and Bi$_{0.95}$Eu$_{0.05}$PO$_4$·xH$_2$O nanoparticles were synthesized by a polyol-mediated method employing diethylene glycol. The powder X-ray diffraction revealed the phase purity and isostructural nature of both undoped and Eu^{3+}-doped BiPO$_4$. The monoclinic Bi$_{0.95}$Eu$_{0.05}$PO$_4$ was obtained by heating the hexagonal Bi$_{0.95}$Eu$_{0.05}$PO$_4$·xH$_2$O at 600 °C. The microscopical characterization revealed the formation of nanocrystalline materials. Water molecules present in the bismuth precursor favoured the formation of hexagonal phase at low temperature. The role of DEG molecules in arresting the particle growth during the phase transformation of Bi$_{0.95}$Eu$_{0.05}$PO$_4$ from hexagonal to monoclinic was observed. The synthesized materials were characterized using different spectroscopic techniques such as FT-IR, Raman, ^{31}P MAS-NMR, DRUV-Vis and PL. The difference in the crystal structures and symmetries is clearly reflected in the spectral results of hexagonal and monoclinic Bi$_{0.95}$Eu$_{0.05}$PO$_4$. The structure-property relations were studied to derive its importance from both fundamental and technological aspects.

1 Introduction

BiPO$_4$ is known for its multifarious applications such as catalyst,[1] orthophosphate ion sensor,[2] microwave dielectric,[3] and in separation of radioactive elements.[4] Recent focus on BiPO$_4$ is due to its application as a host lattice for rare earth luminescent centers and as a photocatalyst.[5–8] BiPO$_4$ crystallizes in three different structures with hexagonal and monoclinic (low and high temperature modifications) symmetries.[9,10] All the three phases of BiPO$_4$ consist of three dimensional network structure made up of PO$_4$ tetrahedra and BiO$_8$ polyhedra. The most stable form is the low temperature monoclinic monazite-type (LTBP) that can be converted into high temperature monoclinic structure (HTBP) when heated at 700 °C and above. Both LTBP and HTBP have closely related crystal structures. The third form is the hexagonal phase of hydrated BiPO$_4$·xH$_2$O which can be synthesized at room temperature through a wet chemical method.[9] Synthesis of BiPO$_4$ with different morphologies has received considerable research attention in recent times. An urchin-like morphology of monoclinic BiPO$_4$ nanoparticles with rare earth doping was obtained by hydrothermal method for its application in high performance luminescent devices.[6] Monoclinic BiPO$_4$ nanowires were obtained by the decomposition of single source precursor tris-chelated diselenophosphato

complex.[11] Monoclinic BiPO$_4$ and BiPO$_4$:Tb^{3+} were synthesized by polyol-mediated method and the Tb^{3+} photoluminescence (PL) emission intensity was found to increase with increasing post annealing temperatures.[5] Hexagonal BiPO$_4$ nanorods were obtained by a sonochemical method without the assistance of surfactant or ligands.[12] Recently, the hexagonal BiPO$_4$ nanorods have been synthesized by electrochemical anodization of Bi metal substrate and its PL property has been reported.[13]

Recent studies revealing the potential of BiPO$_4$ as a host lattice for rare earth luminescent ions motivated us to study the PL properties of Eu^{3+} in different polymorphs of BiPO$_4$. We used the polyol mediated synthesis which is a simple and versatile technique involving the precipitation of nanocrystalline materials in the presence of a multidendate and high-boiling alcohol such as diethylene glycol (bp 246 °C).[14,15] The alcohols, in addition to their role as solvent, act as stabilizers of nanoparticles by preventing the agglomeration and inhibiting the particle growth. The objectives of this work are: primarily the spectroscopic characterization of the host BiPO$_4$ in its two different polymorphs, namely hexagonal and monoclinic, in the nanoscale and to elucidate their structure–spectral properties correlation. Although these correlations has been carried out in the bulk, a comparative study of the spectral properties of BiPO$_4$ nanoparticles, either undoped or doped, is necessary considering the changes in properties at the nanoscale.[9] Secondly, we chose Eu^{3+} since its emissions are hypersensitive *i.e.*, they strongly depend on the local structural symmetry of the host lattice.[16,17] Understanding the PL properties of Eu^{3+} in hexagonal and monoclinic BiPO$_4$ nanoparticles is of fundamental interest and this may pave way for the improvement of properties by

Functional Materials Division, CSIR-Central Electrochemical Research Institute (CECRI), Karaikudi, 630 006, Tamil Nadu, India.
E-mail: nlnsimha@gmail.com; laksnarasimhan@cecri.res.in
(N. Lakshminarasimhan); Fax: +91-4565-227779.;
Tel: +91-4565-227 550 to 559

controlling the surface-bound species in the nanoscale phosphors, especially for their application in white LED technology. In the present study, we report the synthesis of nanocrystalline hexagonal $BiPO_4 \cdot xH_2O$ and $Bi_{0.95}Eu_{0.05}PO_4 \cdot xH_2O$ by polyol-mediated method and the conversion of hexagonal $Bi_{0.95}Eu_{0.05}PO_4 \cdot xH_2O$ into monoclinic monazite phase by thermal treatment without affecting the particle size. The obtained hexagonal and monoclinic $Bi_{0.95}Eu_{0.05}PO_4$ nanoparticles were characterized by various spectroscopic techniques and the results are compared.

2 Experimental

2.1 Synthesis

The polyol-mediated synthesis procedure adopted in the present study is similar to the one reported by Roming and Feldmann except for the starting materials.[5] In a typical synthesis, 1.6009 g (3.3 mmoles) of $Bi(NO_3)_3 \cdot 5H_2O$ (Merck 98%) was dissolved in 100 ml of diethylene glycol (DEG) (SISCO Research Lab. Pvt. Ltd. 99%) at 60 °C. A solution of phosphate precursor consists of 0.4358 g (3.3 mmoles) of $(NH_4)_2HPO_4$ (Lobachemie 98–100%) in 4 ml dist. H_2O was added into DEG solution containing bismuth nitrate under vigorous stirring. The particles were formed immediately and the solution was heated rapidly to 160 °C and kept at this temperature for 1 h followed by cooling to room temperature under constant stirring. After cooling, 100 ml ethanol was added and stirred for 30 min and centrifuged. The obtained particles were washed several times with ethanol and dried at 100 °C in an air oven for 8–10 h. In the case of $Bi_{0.95}Eu_{0.05}PO_4$, a stoichiometric amount of Eu_2O_3 was initially converted into nitrate by dissolving in conc. HNO_3 and the above synthesis procedure was followed. We obtained about 0.98 g of final product (yield 98%).

2.2 Characterization

Thermogravimetric analysis (TGA) of synthesized materials was carried out in air from 30 to 1000 °C with a heating rate of 20 °C min^{-1} using TA (SDT Q600) instrument. The phase formation and purity were monitored by powder X-ray diffraction (XRD) technique using Cu-Kα radiation (D8 Advance, Bruker). The FT-IR spectra were recorded in the mid-IR region using KBr pellet technique (Tensor 27, Bruker). Laser Raman spectra were recorded using Reninshaw Invia Laser Raman microscope equipment with 633 nm He-Ne Laser source through CCD detector. Solid state ^{31}P magic angle spinning (MAS) NMR spectra were recorded in Bruker Advance 400 spectrometer with a magnetic field of 9.4 T operating at a frequency of 161.98 MHz for ^{31}P nuclei. The ^{31}P MAS-NMR spectra were recorded at different spinning rate of the sample tube ranging between 5000–8000 rpm. The scanning electron micrographs (SEM) were obtained using Hitachi (S-3000H) microscope. The transmission electron microscopic (TEM) images were obtained using FEI Technai 20 G2 microscope. The diffuse reflectance UV-Vis (DRUV-Vis) absorption spectra were recorded using a spectrometer (Cary 500, Varian) and $BaSO_4$ was used as a standard to correct the base line. Photoluminescence (PL) emission spectra of powder samples were recorded using JASCO (FP-6500) spectrophotometer.
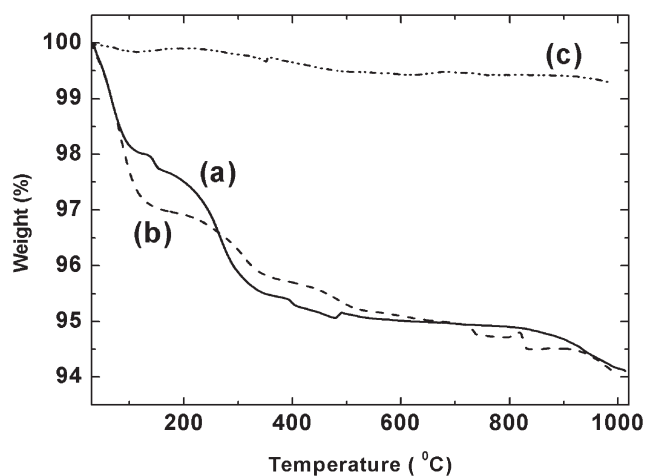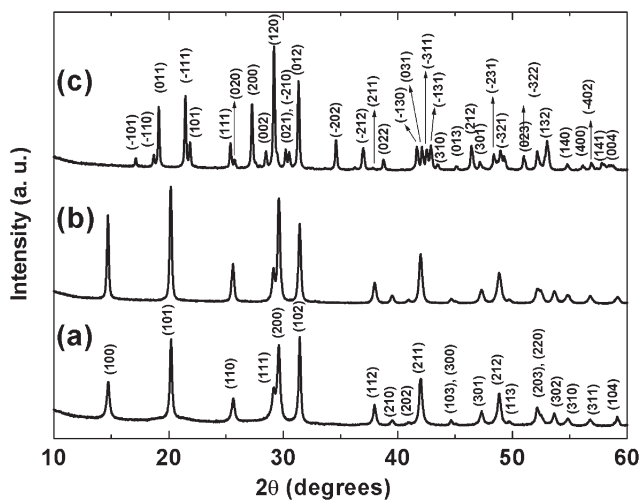

Fig. 1 TGA curves of (a) $BiPO_4 \cdot xH_2O$ (—) and (b) $Bi_{0.95}Eu_{0.05}PO_4 \cdot xH_2O$ (- - - -) as obtained by polyol-mediated synthesis and (c) $Bi_{0.95}Eu_{0.05}PO_4$ (- · · -) obtained after calcinations of (b) at 600 °C/6 h.

3 Results and discussion

3.1 Phase formation

The thermogravimetric analysis (TGA) of the undoped and Eu^{3+}-doped $BiPO_4$ obtained by polyol-mediated method was carried out in order to find the presence of lattice water molecules and the results are shown in Fig. 1a. In the case of $BiPO_4 \cdot xH_2O$, a weight loss ($\sim 2\%$) from room temperature to 150 °C was observed and this could be due to the removal of adsorbed water and ethanol over the particle surface.[10] Another major weight loss was observed between 200 and 350 °C and this could be due to the removal of zeolitic lattice water molecules present in the open channels of hexagonal $BiPO_4 \cdot xH_2O$ structure and some residual DEG which was used as the solvent and capping agent in the synthesis.[18] The TGA result of $Bi_{0.95}Eu_{0.05}PO_4 \cdot xH_2O$ shows almost a similar behaviour (Fig. 1b). Thus, the thermogravimetric analysis revealed the presence of zeolitic lattice water molecules and the residual organics in the sample as obtained by polyol-mediated method. There is no weight change after ~ 550 °C and hence the calcination of hexagonal $Bi_{0.95}Eu_{0.05}PO_4 \cdot xH_2O$ was carried out at 600 °C above which the conversion into high temperature monoclinic phase may occur.[3] The TGA result of $Bi_{0.95}Eu_{0.05}PO_4$ obtained by heat treatment of hexagonal phase at 600 °C/6 h (Fig. 1c) shows a negligible weight loss ($<1\%$) which could be due to adsorbed moisture. This result clearly reveals the complete removal of zeolitic water molecules and residual organics during the phase transformation of hexagonal $Bi_{0.95}Eu_{0.05}PO_4 \cdot xH_2O$ into monoclinic $Bi_{0.95}Eu_{0.05}PO_4$ by thermal treatment.

The powder XRD patterns of $BiPO_4 \cdot xH_2O$ and $Bi_{0.95}Eu_{0.05}PO_4 \cdot xH_2O$ samples as obtained by polyol-mediated method are shown in Fig. 2a and 2b, respectively. All the reflections were indexed based on hexagonal symmetry with reference to the standard pattern available in the JCPDS data base (No. 15-0766). The single phase formation of both $BiPO_4 \cdot xH_2O$ and $Bi_{0.95}Eu_{0.05}PO_4 \cdot xH_2O$ is clearly evident from the fact that there are no unidentified reflections in the XRD patterns. The similarity in the powder XRD patterns of $BiPO_4 \cdot xH_2O$ and $Bi_{0.95}Eu_{0.05}PO_4 \cdot xH_2O$ reveals their isostructural nature. The calculated hexagonal lattice parameters are listed in Table 1 and

Fig. 2 Powder XRD patterns of (a) $BiPO_4 \cdot xH_2O$, (b) $Bi_{0.95}Eu_{0.05}PO_4 \cdot xH_2O$ as obtained by polyol-mediated method and (c) $Bi_{0.95}Eu_{0.05}PO_4$ obtained by calcination of (b) at 600 °C.

Table 1 Calculated lattice parameters of $BiPO_4$ and $Bi_{0.95}Eu_{0.05}PO_4$

Lattice parameters	$BiPO_4{}^a$	$Bi_{0.95}Eu_{0.05}PO_4$	
		Hexagonal^a	Monoclinic^b
'a' (Å)	6.9841(2)	6.9790(1)	6.7521(2)
'b' (Å)	6.9841(2)	6.9790(1)	6.9385(1)
'c' (Å)	6.4755(2)	6.4702(2)	6.4690(2)

^{a} $\alpha = \beta = 90.00°$, $\gamma = 120.00°$. ^{b} $\alpha = 90.00°$, $\beta = 103.71°$, $\gamma = 90.00°$.

values of $BiPO_4 \cdot xH_2O$ are in good agreement with the values available in JCPDS file. There is a marginal decrease in both 'a' and 'c' lattice parameters in the case of $Bi_{0.95}Eu_{0.05}PO_4 \cdot xH_2O$ when compared to $BiPO_4$ which is due to the smaller ionic radius of Eu^{3+} (1.07 Å) than that of Bi^{3+} (1.11 Å) in 8-fold coordination.[19] The intense and broader reflections in the powder XRD patterns reveal the formation of the nanocrystallites. The crystallite sizes were calculated from the full width at half maximum (FWHM) of selected reflections using Scherrer's formula.[20] In the case of $BiPO_4 \cdot xH_2O$, the calculated crystallite sizes corresponding to the (100) and (110) reflections are 51 and 46 nm, respectively. Similar crystallite sizes were obtained for $Bi_{0.95}Eu_{0.05}PO_4 \cdot xH_2O$. Thus, the polyol-mediated synthesis yielded the nanocrystalline hexagonal $BiPO_4 \cdot xH_2O$ and $Bi_{0.95}Eu_{0.05}PO_4 \cdot xH_2O$ since a low temperature was involved in the synthesis.

The hexagonal $BiPO_4 \cdot xH_2O$ is known to form at room temperature with associated lattice water molecules (x = 0.5–0.67).[9,10] Hexagonal $BiPO_4$ consists of an open framework structure due to the symmetrical arrangement of chain of alternating BiO_8 polyhedra and PO_4 tetrahedra with zeolitic water molecules located in the channels parallel to 'c' axis as shown in Fig. 3a.[9] In the case of monoclinic $BiPO_4$, the chains are less symmetrically arranged and hence the structure consists of a compact space-filling network (Fig. 3c). Most of the reports on $BiPO_4$ deals with the monoclinic phase since the syntheses were performed at relatively high temperatures. In the present study, $BiPO_4$ was synthesized following the procedure described by Roming and Feldmann.[5] However, the hexagonal $BiPO_4$ has

been obtained in the present study whereas the monoclinic phase was obtained by Roming and Feldmann. The reason for this could be the difference in the bismuth precursors used in both these studies. BiI_3 was used by Roming and Feldmann whereas $Bi(NO_3)_3 \cdot 5H_2O$ has been used in the present study. The presence of water molecules in the starting material could lead to the formation of hexagonal $BiPO_4 \cdot xH_2O$. The structurally analogous hexagonal $LnPO_4 \cdot xH_2O$ [Ln = La, Ce, Nd, Sm, Eu, Gd and Tb] nanorods were synthesized starting from aqueous solutions of Ln(III) nitrates and $NH_4H_2PO_4$ under solvothermal conditions in a microwave oven in which the aqueous condition might favor the formation of hexagonal phase.[21] To confirm the role of water molecules, we carried out the polyol-mediated synthesis in which the $Bi(NO_3)_3 \cdot 5H_2O$ in DEG was initially heated at 150 °C for 30 min in order to remove the water molecules present in the precursor. Then, the aqueous solution of $(NH_4)_2HPO_4$ (4 ml) was carefully added to get the final product by the method as described in the experimental section. The powder XRD pattern of this sample (Fig. 4) revealed the presence of monoclinic $BiPO_4$ as major phase and hexagonal $BiPO_4$ as minor phase. The presence of additional hexagonal $BiPO_4$ could be due to the trace amount of water remaining either in the bismuth precursor solution or from the aqueous solution of $(NH_4)_2HPO_4$. However, the water in the phosphate precursor may not influence the phase formation as Roming and Feldmann used aqueous phosphate precursor in their synthesis of monoclinic $BiPO_4$:Tb. This result substantiates that the water molecules associated with the bismuth precursor favours the formation of hexagonal $BiPO_4$ rather than the monoclinic $BiPO_4$ as obtained with non-aqueous precursor BiI_3.[5] A similar strategy has been adopted in the direct precipitation of monoclinic $LaPO_4$.[22] The water containing precursor $La(NO_3)_3 \cdot 6H_2O$ was added to hot H_3PO_4 solution kept at 150 °C in order to avoid the participation of water molecules which would otherwise lead to the formation of hexagonal $LaPO_4 \cdot 0.5H_2O$. Another possible reason for the formation of hexagonal $BiPO_4$ could be the use of acidic $Bi(NO_3)_3 \cdot 5H_2O$ precursor as the acidic environment favours the formation of hexagonal $BiPO_4 \cdot xH_2O$.[9]

In order to convert the hexagonal $Bi_{0.95}Eu_{0.05}PO_4 \cdot xH_2O$ into low temperature monoclinic phase and also to remove the zeolitic lattice water molecules and residual DEG molecules, the sample was calcined at 600 °C for 6 h. This temperature was chosen based on the thermogravimetric result that is shown in Fig. 1. In analogues $LnPO_4 \cdot xH_2O$ [Ln = La and Ce], the hexagonal to low temperature monoclinic phase transition has been found by *in situ* high temperature XRD to occur at about 600 °C.[23] Calcination of $Bi_{0.95}Eu_{0.05}PO_4 \cdot xH_2O$ at 600 °C resulted in the phase transformation from hexagonal to low temperature monoclinic phase of $Bi_{0.95}Eu_{0.05}PO_4$ as evident from the powder XRD (Fig. 2c) and all the reflections were indexed based on the standard pattern (JCPDS 015-0767). The zeolitic water molecules present in the open channels stabilize the hexagonal structure and the removal of which results in the irreversible transformation of the phase to low temperature monoclinic $BiPO_4$ structure.[10] The calculated lattice parameters (Table 1) of $Bi_{0.95}Eu_{0.05}PO_4$ revealed a marginal decrease when compared to the lattice parameters available with standard pattern of undoped monoclinic $BiPO_4$ and this is due to the substitution of Bi^{3+} by smaller Eu^{3+} ion. The calculated crystallite sizes of

(a)

(b)

(c)

(d)
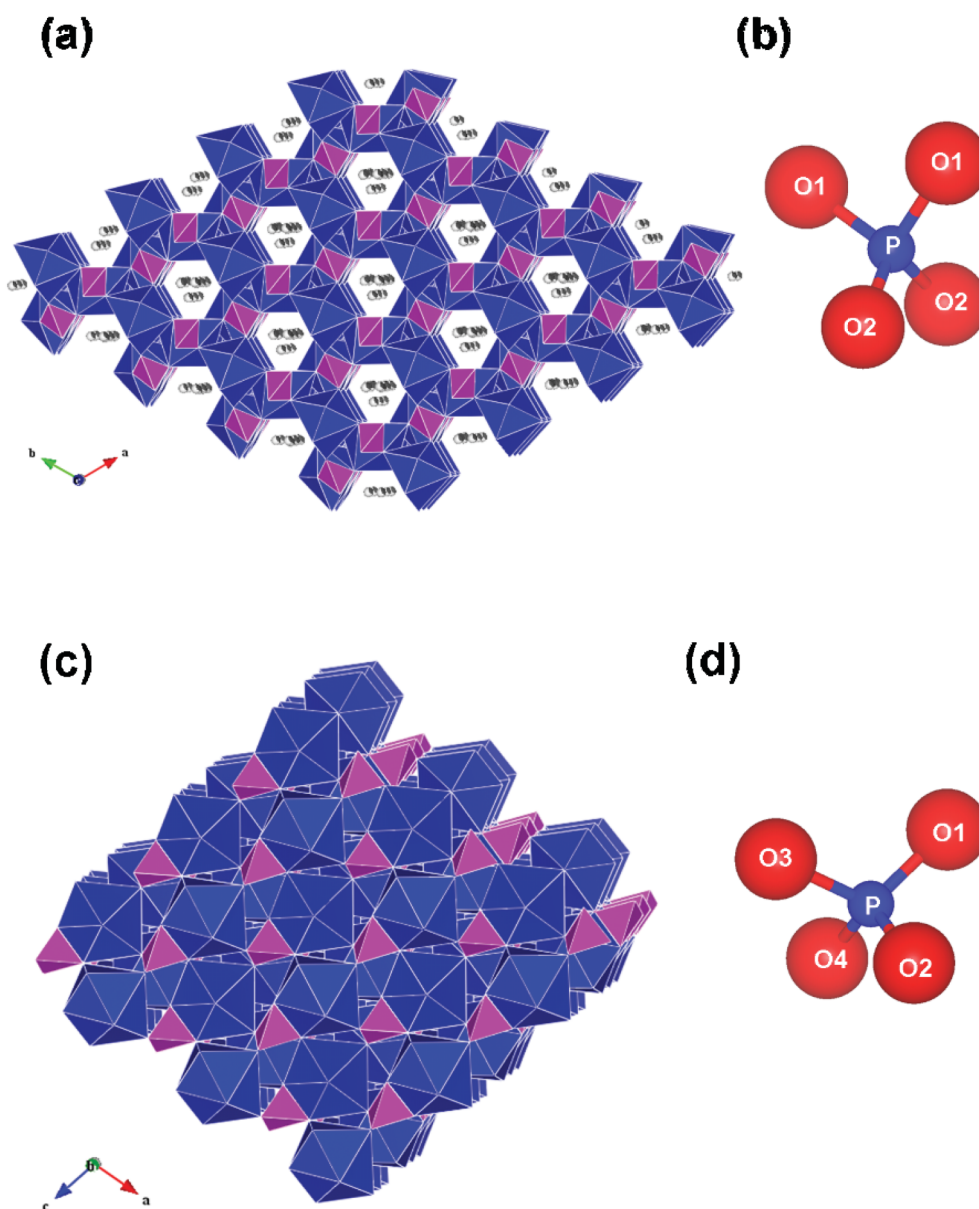
Fig. 3 Crystal structures of (a) hexagonal $BiPO_4 \cdot xH_2O$ (with H_2O molecules shown inside the channels) and (c) low-temperature monoclinic $BiPO_4$ with BiO_8 polyhedra (dark blue) and PO_4 tetrahedra (majenta). The $-PO_4$ tetrahedron of (b) hexagonal and (d) monoclinic $BiPO_4$ are shown. Crystal structures are drawn using VESTA program[40] using the atomic coordinates given in ref. 9.

monoclinic $Bi_{0.95}Eu_{0.05}PO_4$ from the FWHM of the reflections (200) and (012) using Scherrer's formula are 48 and 51 nm, respectively. This result shows that the calcination process had no influence on the particle growth which will be discussed in a later section.

3.2 Morphological analysis

The morphologies of undoped and Eu^{3+} doped $BiPO_4 \cdot xH_2O$ were analyzed by scanning and transmission electron microscopic techniques and the images are shown in Fig. 5 and 6, respectively. The SEM images of $BiPO_4 \cdot xH_2O$ and $Bi_{0.95}Eu_{0.05}PO_4 \cdot xH_2O$ (Fig. 5a and 5b) show that the particles are cocoon-like in shape and are uniformly distributed. The length of each cocoon is of 1 µm and the width is around 500 nm. A similar morphology of hexagonal $BiPO_4$ was obtained by hydrothermal synthesis using glycerol/water solvent and the size of the nano-cocoons was

around 100–150 nm.[24] Based on the crystallite size calculated from the XRD results ($\sim$ 50 nm), it is assumed that each micron sized cocoon is made up of compactly packed smaller primary nanoparticles of the size less than 100 nm. In order to observe this feature clearly, TEM analysis was carried out and from the images (Fig. 6a and 6b) it is clearly seen that the individual particles of sizes less than 50 nm are packed inside the cocoon-like secondary particles. An envelope of organic layer is seen over the particles and this could be the residual surface bound DEG. This result confirms that the primary particles are smaller in size of about 50 nm and correlates well with the crystallite sizes calculated from the powder XRD patterns of $BiPO_4$ and $Bi_{0.95}Eu_{0.05}PO_4 \cdot xH_2O$. The morphology of monoclinic $Bi_{0.95}Eu_{0.05}PO_4$ has changed from the cocoon-like larger particles into clusters of spherical nanoparticles as observed in SEM image (Fig. 5c). Further, the TEM image of
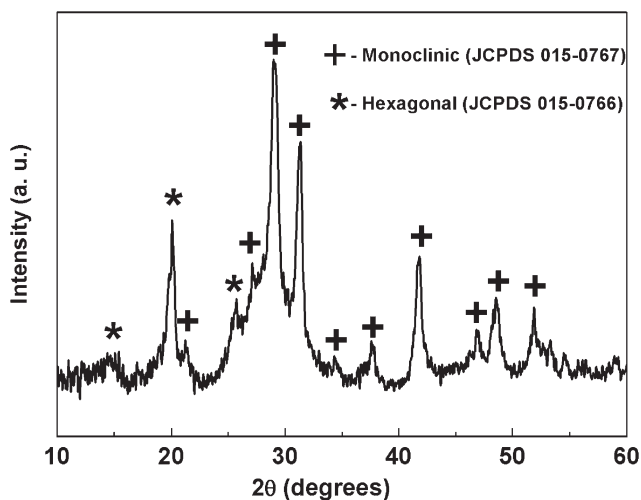
Fig. 4 Powder XRD pattern of $BiPO_4$ obtained by polyol-mediated method with heating the precursor $Bi(NO_3)_3\cdot5H_2O$ in DEG at 150 °C to remove H_2O. The pattern contains both monoclinic $BiPO_4$ (+, major phase) and hexagonal $BiPO_4$ (* minor phase).

monoclinic $Bi_{0.95}Eu_{0.05}PO_4$ (Fig. 6c) shows the random aggregates of nanoparticles with the size ranging from 20 to 100 nm. These results clearly reveal that the effect of calcination (600 °C/6 h) is only on the morphology (arrangement of nanoparticles) and not on the particle size. This could be attributed to the presence of DEG that prevents the particle growth.

3.3 Role of DEG

In the polyol-mediated synthesis of undoped and Eu^{3+}-doped $BiPO_4$ nanoparticles, the DEG acts both as a solvent and a capping agent that prevents the primary nanoparticles to aggregate in a random fashion. DEG assisted in assembling the primary nanoparticles in a uniform manner to form a cocoon-like morphology. To confirm this, a simple precipitation

of $BiPO_4$ was carried out by adding diammonium hydrogen phosphate solution to an aqueous solution of bismuth nitrate at 80 °C to obtain the $BiPO_4$ particles. The formation of hexagonal $BiPO_4\cdot xH_2O$ was confirmed from the powder XRD result (Fig. S1, ESI)†. The XRD pattern contained sharp and intense reflections revealing a highly crystalline material. The SEM image (Fig. S2, ESI)† showed the presence of large particles (0.2–1.0 μm) with random shapes varying from brick-like to irregular ones. This result confirms the role of DEG as a capping agent in preventing the random aggregation of primary $BiPO_4$ nanoparticles and limiting the particle growth during the polyol-mediated synthesis. Further, on heat treatment at 600 °C for 6 h, the hexagonal $Bi_{0.95}Eu_{0.05}PO_4\cdot xH_2O$ converted into monoclinic $Bi_{0.95}Eu_{0.05}PO_4$ by the removal of zeolitic water molecules as well as the surface bound DEG molecules. The thermal treatment also changed the morphology from the cocoon-like secondary particles into random aggregates of primary nanoparticles (Fig. 5c and more TEM images in Fig. S3 and S4, ESI† depicting the hexagonal $Bi_{0.95}Eu_{0.05}PO_4\cdot xH_2O$ and monoclinic $Bi_{0.95}Eu_{0.05}PO_4$ respectively). This result suggests that the removal of surface bound DEG molecules on heating leads to the rupture of cocoons and the spill out of the primary nanoparticles from the cocoons to form the random and non-uniform spherical aggregates as depicted schematically in Fig. 7.

3.4 Spectral properties

The FT-IR spectra of hexagonal $BiPO_4\cdot xH_2O$, $Bi_{0.95}Eu_{0.05}PO_4\cdot xH_2O$ and monoclinic $Bi_{0.95}Eu_{0.05}PO_4$ are shown in Fig. 8. The absorption band at 1022 cm^{-1} corresponds to the asymmetric stretching (ν_3) vibration and the bands at 598 and 544 cm^{-1} are due to the asymmetric bending vibrations (ν_4) of $-PO_4$ group.[25] The observed ν_3 absorption bands of hexagonal $BiPO_4\cdot xH_2O$, $Bi_{0.95}Eu_{0.05}PO_4\cdot xH_2O$ (Fig. 8a and 8b) are more symmetric without any splitting when compared to that of monoclinic $Bi_{0.95}Eu_{0.05}PO_4$ in which a splitting into four absorption bands is observed (Fig. 8c). Our result is similar to the one reported in the literature.[10] The $-PO_4$
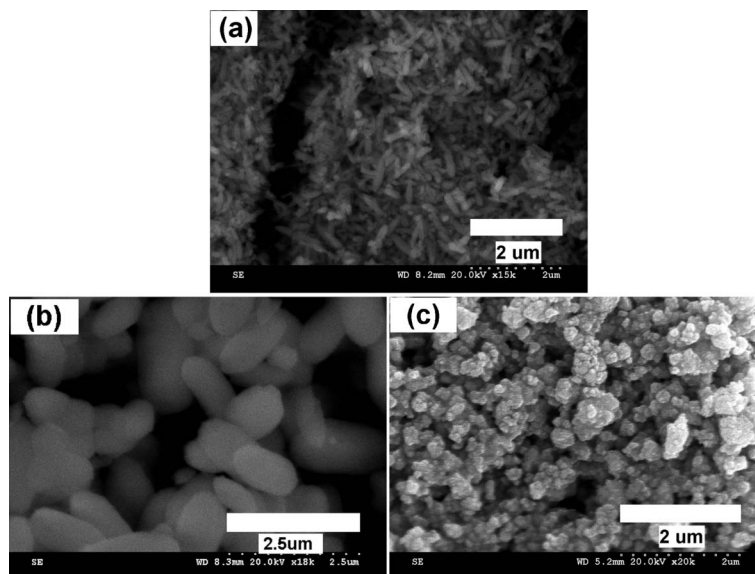
Fig. 5 SEM images of hexagonal (a) $BiPO_4\cdot xH_2O$, (b) $Bi_{0.95}Eu_{0.05}PO_4\cdot xH_2O$ as obtained by polyol-mediated method and (c) monoclinic $Bi_{0.95}Eu_{0.05}PO_4$.
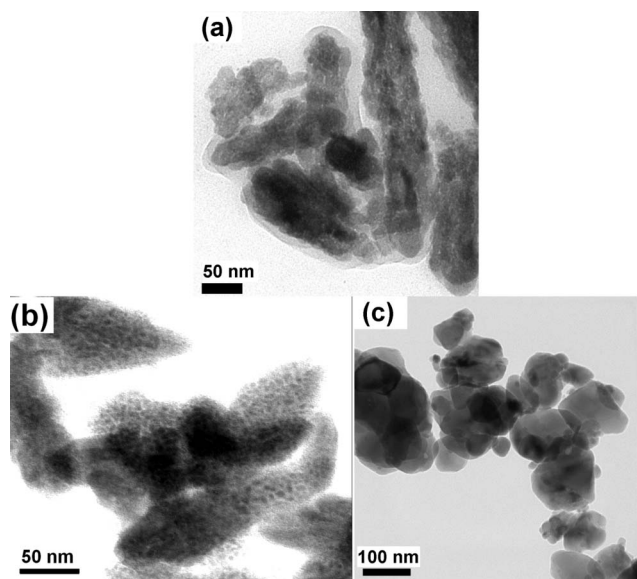
Fig. 6 TEM images of hexagonal (a) $BiPO_4 \cdot xH_2O$, (b) $Bi_{0.95}Eu_{0.05}PO_4 \cdot xH_2O$ as obtained by polyol-mediated method and (c) monoclinic $Bi_{0.95}Eu_{0.05}PO_4$.
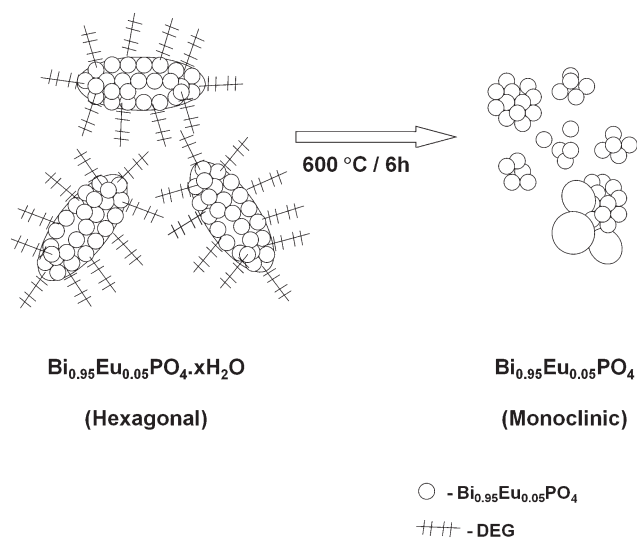

Fig. 7 Schematic illustration showing the conversion of cocoon-like morphology of $Bi_{0.95}Eu_{0.05}PO_4$ stabilized by DEG into random spherical aggregates by heating at 600 °C by loss of DEG.

group in hexagonal $BiPO_4 \cdot xH_2O$ has C_2 symmetry with two different P–O bond lengths (1.5406 and 1.5341 Å) and it could be considered to have a pseudo-tetrahedral symmetry.[10] The symmetry of –PO_4 group in monoclinic $BiPO_4$ is C_1 since all the four P–O bonds are different with lengths varying between 1.4684 and 1.5368 Å. This difference in the symmetry of the –PO_4 group resulted in the observed difference in the FT-IR spectra of hexagonal and monoclinic $Bi_{0.95}Eu_{0.05}PO_4$. The absorptions at 3450 and 1620 cm^{-1} are due to the –OH stretching and HOH bending vibrations, respectively, of lattice water in undoped and Eu^{3+}-doped $BiPO_4 \cdot xH_2O$.[24] The absorption bands observed between 2800 and 3000 cm^{-1} correspond to the stretching vibrations of C–H bonds of DEG.[26] These results indicate that
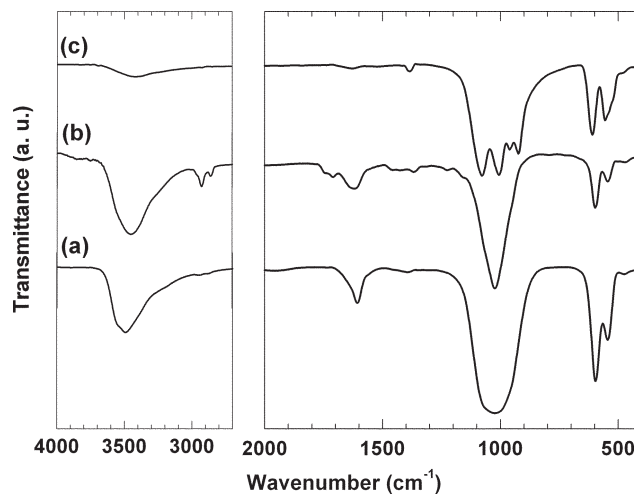

Fig. 8 FT-IR spectra of hexagonal (a) $BiPO_4 \cdot xH_2O$ and (b) $Bi_{0.95}Eu_{0.05}PO_4 \cdot xH_2O$ as obtained by polyol-mediated method; (c) monoclinic $Bi_{0.95}Eu_{0.05}PO_4$ obtained after calcination of (b) at 600 °C.

the DEG molecules are adsorbed over the surface of $BiPO_4 \cdot xH_2O$ and $Bi_{0.95}Eu_{0.05}PO_4 \cdot xH_2O$ samples and are in agreement with the TGA results. A weak absorption band observed at ∼3400 cm^{-1} in monoclinic $Bi_{0.95}Eu_{0.05}PO_4$ could be due to adsorbed moisture. Thus, the calcination of hexagonal $Bi_{0.95}Eu_{0.05}PO_4 \cdot xH_2O$ converted it into monoclinic $Bi_{0.95}Eu_{0.05}PO_4$ with the removal of zeolitic lattice water molecules.

The laser Raman spectra of hexagonal $BiPO_4 \cdot xH_2O$ and $Bi_{0.95}Eu_{0.05}PO_4 \cdot xH_2O$ and monoclinic $Bi_{0.95}Eu_{0.05}PO_4$ are shown in Fig. 9a–c. Broad bands were observed with the hexagonal $BiPO_4 \cdot xH_2O$ and $Bi_{0.95}Eu_{0.05}PO_4 \cdot xH_2O$ samples and this could be due to the presence of zeolitic water molecules and the residual organics. The Raman spectrum of monoclinic $Bi_{0.95}Eu_{0.05}PO_4$ contains relatively narrow bands which are clearly distinguishable from the hexagonal phase. In all the three spectra, the observed intense line at 170 cm^{-1} and a shoulder at 231 cm^{-1} are due to the stretching vibration modes of heavy metal ion, Bi^{3+} (Bi–O), in BiO_8 polyhedron.[27,28] The
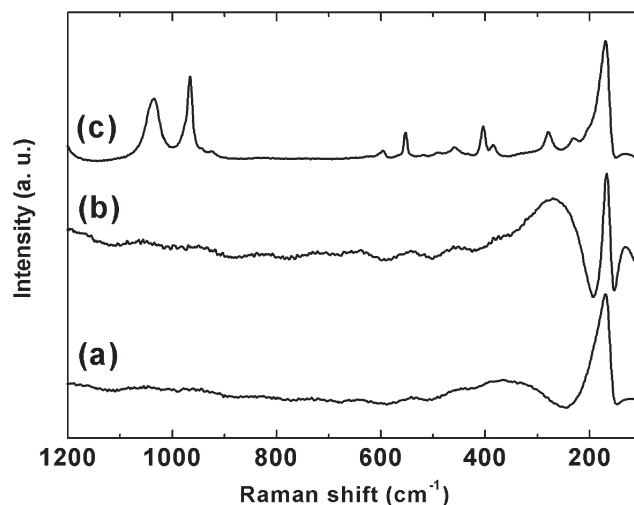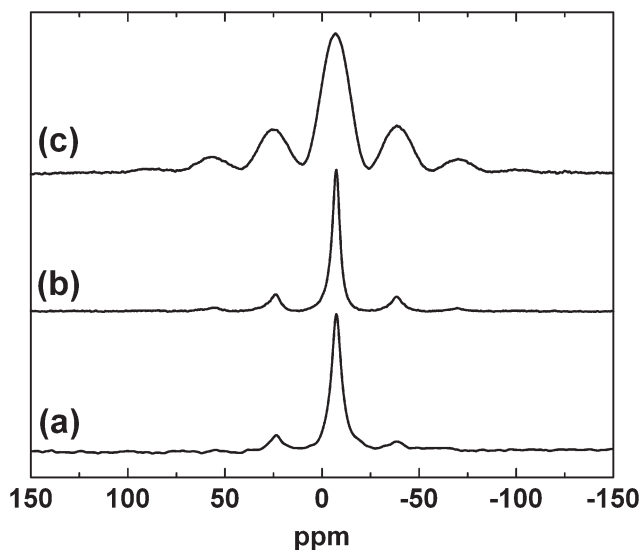

Fig. 9 Laser Raman spectra of hexagonal (a) $BiPO_4 \cdot xH_2O$, (b) $Bi_{0.95}Eu_{0.05}PO_4 \cdot xH_2O$ and (c) monoclinic $Bi_{0.95}Eu_{0.05}PO_4$.

Fig. 10 ^{31}P MAS-NMR spectra of hexagonal (a) $BiPO_4 \cdot xH_2O$, (b) $Bi_{0.95}Eu_{0.05}PO_4 \cdot xH_2O$ and (c) monoclinic $Bi_{0.95}Eu_{0.05}PO_4$.

Peaks at 1035 and 966 cm^{-1} are due to the asymmetric (ν_3) and symmetric (ν_1) stretching vibrations of the –PO$_4$ group, respectively. The bands in the region between 550 and 600 cm^{-1} correspond to the ν_4 bending vibration modes of –PO$_4$ groups.[12] The weak bands at 403 and 458 cm^{-1} can be assigned to the ν_2 bending vibration of –PO$_4$ units. Though the structural symmetry difference between hexagonal and monoclinic $Bi_{0.95}Eu_{0.05}PO_4$ has been reflected in the FT-IR spectral results, we could not find the difference in the Raman spectra due to the observed broadness in the spectra of both undoped and Eu^{3+}-doped hexagonal $BiPO_4$.

We, for the first time, report here the ^{31}P MAS-NMR spectral results of hexagonal as well as monoclinic $BiPO_4$ and attempted to reason out the difference observed between them. The ^{31}P MAS-NMR spectra of hexagonal $BiPO_4 \cdot xH_2O$, $Bi_{0.95}Eu_{0.05}PO_4 \cdot xH_2O$, and monoclinic $Bi_{0.95}Eu_{0.05}PO_4$ are shown in Fig. 10a–c, respectively. Only one line is expected for ^{31}P nucleus in a given site since the nuclear spin (I) is ½. The NMR spectra consisted of one major signal flanked by small bands. The small bands were identified as spinning side bands since their positions uniformly shifted when the spectra were recorded under different spinning rates (see Fig. S5 in ESI)†.[29] However, the position of the major signal remained unaltered and this result reveals that ^{31}P exhibits only one signal in both undoped and Eu^{3+}-doped $BiPO_4$ with hexagonal and monoclinic structures. This result is also in agreement with the crystal structure of $BiPO_4$ in which the P atom occupies only one crystallographic site.[9,10] The chemical shifts observed with the major line are −7.39 and −7.21 ppm for hexagonal $BiPO_4 \cdot xH_2O$ and $Bi_{0.95}Eu_{0.05}PO_4 \cdot xH_2O$, respectively. The chemical shift of the major line of monoclinic $Bi_{0.95}Eu_{0.05}PO_4$ is −6.88 ppm. The major difference between the hexagonal and monoclinic $Bi_{0.95}Eu_{0.05}PO_4$ is the broadness in the signal as well as the appearance and intensities of spinning side bands. The ^{31}P MAS-NMR signal of monoclinic $Bi_{0.95}Eu_{0.05}PO_4$ is broader than that of hexagonal phase. The relative intensities of spinning side bands are higher with the monoclinic $BiPO_4$ when compared with the hexagonal phase. In general, the NMR signal in the solid state

is broad due to the anisotropic nature in the spin–lattice and spin–spin relaxation processes and the relaxation is predominantly by spin–spin interaction.[30] The FWHM values of the main signal of hexagonal $Bi_{0.95}Eu_{0.05}PO_4 \cdot xH_2O$ and monoclinic $Bi_{0.95}Eu_{0.05}PO_4$ are 754 and 2729 Hz, respectively. This shows that there is a difference in the spin–spin and/or spin–lattice relaxation. The presence of zeolitic water molecules and residual DEG may play a role in the case of hexagonal $Bi_{0.95}Eu_{0.05}PO_4$. The broadening of ^{31}P MAS-NMR signal was observed in analogous hexagonal $LaPO_4 \cdot 0.5H_2O$ during its conversion into anhydrous hexagonal phase and finally to monoclinic $LaPO_4$ upon heating.[23] This broadening was attributed to the increase in the distribution of –PO$_4$ tetrahedron local environments in the monoclinic structure. In the present study, the difference in FWHM of NMR signal between hexagonal $Bi_{0.95}Eu_{0.05}PO_4 \cdot xH_2O$ and monoclinic $Bi_{0.95}Eu_{0.05}PO_4$ could be due to the difference in the crystal structure and symmetry. The internuclear distance between ^{31}P nuclei are different in hexagonal (4.1802 Å) and monoclinic (4.0294 and 5.3535 Å) $BiPO_4$.[10] Hence, there could be anisotropic relaxation of spins in monoclinic $BiPO_4$ due to the two different P–P distances and this may result in the observed broadening of the NMR signal. The surface bound DEG molecules stabilize the hexagonal $Bi_{0.95}Eu_{0.05}PO_4 \cdot xH_2O$ nanoparticles in the form of cocoons and due to this the spin–spin relaxation between ^{31}P nuclei in nanoparticles of different cocoons becomes less efficient leading to narrow spectrum. On the other hand, in monoclinic $Bi_{0.95}Eu_{0.05}PO_4$, the relaxation between ^{31}P nuclei of different nanoparticles among the random aggregates may be more efficient resulting in the broad spectrum. A detailed measurement of the relaxation times and theoretical NMR spectral simulations may provide a better understanding of the observed broadening of signal in the ^{31}P MAS-NMR spectra.

3.5 Optical properties

The optical properties of undoped and Eu^{3+}-doped $BiPO_4$ samples were studied by DRUV-Vis absorption and PL spectroscopic techniques. The DRUV-Vis absorption spectra of hexagonal $BiPO_4 \cdot xH_2O$, $Bi_{0.95}Eu_{0.05}PO_4 \cdot xH_2O$, and monoclinic $Bi_{0.95}Eu_{0.05}PO_4$ are shown in Fig. 11. In all the three spectra, the absorption band shows a splitting with the maxima around 225 and 255 nm. Such absorptions in the UV region originate mainly from the optical transitions $^1S_0 \rightarrow {}^1P_1$ and $^1S_0 \rightarrow {}^3P_1$ of $6s^2$ lone pair cation Bi^{3+}.[31] From Fig. 11, it is clear that the absorption onset lies in the UV region at ~320 nm and there is no difference in the absorption onset between hexagonal and monoclinic $Bi_{0.95}Eu_{0.05}PO_4$. The estimated optical band gap [inset (i) in Fig. 11] for $BiPO_4$ from the Kubelka-Munk function is 3.90 eV which is in close agreement with the literature report (3.85 eV).[7] A closer look at the absorption spectrum of monoclinic $Bi_{0.95}Eu_{0.05}PO_4$ reveals a shoulder at around 290 nm. This could be due to the Eu^{3+}–O^{2-} charge transfer (c.t.) absorption band. In order to find this more clearly, the spectrum was deconvoluted into three bands with the absorption maxima at 222, 255 and 285 nm. This clearly reveals the presence of both Bi^{3+} as well as Eu^{3+} absorption bands which is in good agreement with the analysis by Blasse according to which the optical absorptions of Bi^{3+} (S–P transition) and Eu^{3+} (Eu^{3+}–O^{2-} c.t.) occur closely in the UV region.[31]
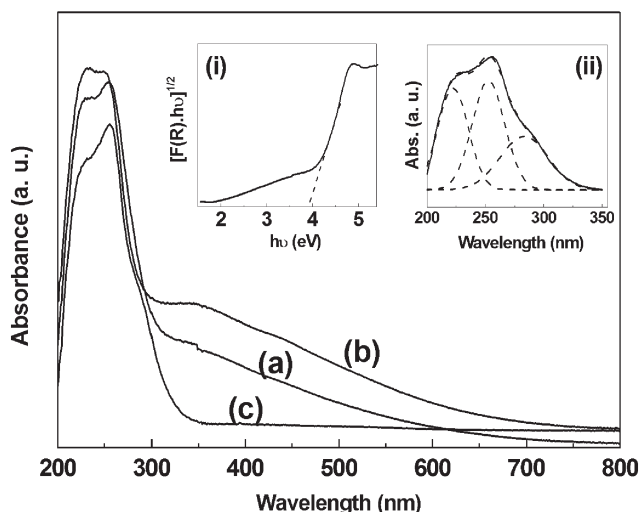
**Fig. 11** Diffuse reflectance UV-Vis absorption spectra of hexagonal (a) $BiPO_4 \cdot xH_2O$, (b) $Bi_{0.95}Eu_{0.05}PO_4 \cdot xH_2O$ and (c) monoclinic $Bi_{0.95}Eu_{0.05}PO_4$. The insets (i) the Kubelka-Munk function revealing the optical band gap of hexagonal $BiPO_4$ and (ii) the deconvolution of absorption spectrum of monoclinig $Bi_{0.95}Eu_{0.05}PO_4$ revealing three absorption bands.

In the case of hexagonal $BiPO_4 \cdot xH_2O$ and $Bi_{0.95}Eu_{0.05}PO_4 \cdot xH_2O$, an enhanced absorption in the visible region from 400 to 700 nm is observed and such absorption is completely absent in monoclinic $Bi_{0.95}Eu_{0.05}PO_4$. This could be due to the presence of residual DEG molecular species over the surface of the phosphate nanoparticles which is also evident from the FT-IR spectroscopic results. There is a possibility of formation of composite of $BiPO_4$ and organic DEG molecular species through phosphate ester linkage. Recently in the literature, a similar additional broad absorption in the region between 290 and 550 nm has been observed in the DRUV-Vis spectrum of $LaPO_4:Eu^{3+}$ nanorods capped with oleic acid (OA).[32] This additional absorption has been attributed to the formation of midgap states due to the chemical bonding between OA and $LaPO_4:Eu^{3+}$. A similar interaction between residual DEG and $BiPO_4$ may result in such enhanced absorption in the visible region for hexagonal $BiPO_4 \cdot xH_2O$ and $Bi_{0.95}Eu_{0.05}PO_4 \cdot xH_2O$ in the present study. However, the exact reason for the origin of such absorption is not clear at this moment. The calcination step (600 °C/6 h.) involved in the synthesis of monoclinic $Bi_{0.95}Eu_{0.05}PO_4$ resulted in the complete removal of DEG molecules and hence the disappearance of visible light absorption in the DRUV-Vis spectrum of this sample. The presence of visible light absorption in hexagonal $Bi_{0.95}Eu_{0.05}PO_4 \cdot xH_2O$ may either enhance the PL emission properties through sensitization or diminish the emission from Eu^{3+} by blocking the light absorption by the active center. The influence of such absorption on the PL properties is discussed below.

We recorded the PL excitation and emission spectra of monoclinic $Bi_{0.95}Eu_{0.05}PO_4$ obtained by conventional solid state reaction method as a reference (Fig. S6 in ESI)†. The excitation spectrum showed the high intense peak at 395 nm which is due to $^7F_0$-$^5L_6$ absorption of Eu^{3+}. We did not observe any emission from the host $BiPO_4$ and this result is in agreement with the literature report.[5] The PL emission spectrum of hexagonal $Bi_{0.95}Eu_{0.05}PO_4 \cdot xH_2O$ as obtained by polyol method is shown in

Fig. 12a. The observed emissions of hexagonal $Bi_{0.95}Eu_{0.05}PO_4 \cdot xH_2O$ were due to different emission transitions originating from $^5D_0$ state ($^5D_0 \rightarrow ^7F_{j=0,1,2}$) of Eu^{3+}. However, the emission intensities are very low. The possible reason stems from the DRUV-Vis spectral result in which hexagonal $Bi_{0.95}Eu_{0.05}PO_4 \cdot xH_2O$ exhibited an enhanced absorption in the visible region when compared to that of monoclinic $Bi_{0.95}Eu_{0.05}PO_4$. This absorption from the surface bound DEG molecules resulted in the pale yellow color of hexagonal $BiPO_4 \cdot xH_2O$ and $Bi_{0.95}Eu_{0.05}PO_4 \cdot xH_2O$ samples possibly by the formation of a composite of DEG and $BiPO_4$. Thus, the effective light absorption by Eu^{3+} during excitation may be hindered due to the absorption by surface bound organics which thereby reduces the emission intensity. There are also chances of re-absorption of light emitted by Eu^{3+} in the visible region (550–650 nm) by surface bound DEG molecules resulting in the poor emission intensity. Another possible reason could be the presence of lattice H_2O molecules and the residual DEG in the sample which could quench the PL emission through a non-radiative emissive transition.[33,34] In the case of $BiPO_4:Tb^{3+}$ synthesized by polyol-method using DEG, an enhancement in the emission intensity was observed with increase in the calcination temperature.[5] We believe that this could be due to the complete removal of the surface bound DEG molecules by calcination. Our results also reveal that the surface bound DEG molecules have a deteriorating effect on the PL emission of $Bi_{0.95}Eu_{0.05}PO_4 \cdot xH_2O$ despite its role as a stabilizer of the nanoparticles. The PL emission spectrum of monoclinic $Bi_{0.95}Eu_{0.05}PO_4$ obtained by calcination of hexagonal sample is shown in Fig. 12b. We could clearly observe the enhancement in the intensity of orange emission caused by the magnetic dipole transition $^5D_0 \rightarrow ^7F_1$ of Eu^{3+} ion. Due to the difference in the crystal structures and symmetry between hexagonal and monoclinic $BiPO_4$, a difference in the emission spectral feature for $^5D_0 \rightarrow ^7F_1$ transition of Eu^{3+} was observed.[35–37] A difference in the PL emission properties of the hexagonal and monoclinic $EuPO_4$ nanoparticles was previously reported in the literature.[38] The ratio of $^5D_0 \rightarrow ^7F_2 / ^5D_0 \rightarrow ^7F_1$ transitions increased with the loss of water within the hexagonal phase while the emission decreased with the conversion of hexagonal $EuPO_4$ into monoclinic phase. In the
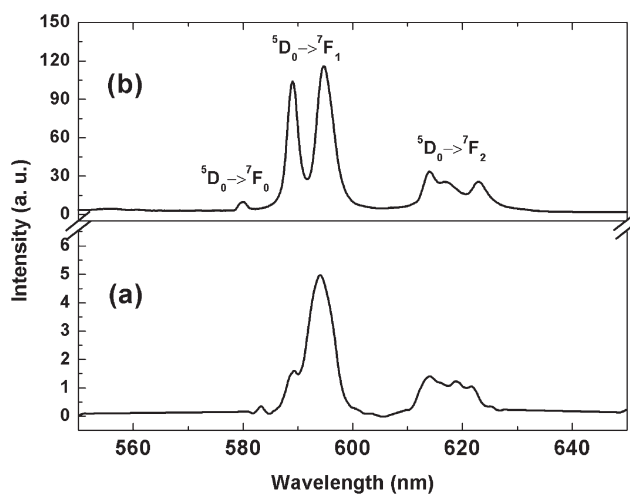
Fig. 12 PL emission spectra ($\lambda_{exc.}$ = 395 nm) of (a) hexagonal $Bi_{0.95}Eu_{0.05}PO_4 \cdot xH_2O$ as obtained by polyol-mediated method and (b) monoclinic $Bi_{0.95}Eu_{0.05}PO_4$ obtained by calcination of (a) at 600 °C.

hexagonal $Bi_{0.95}Eu_{0.05}PO_4 \cdot xH_2O$, a broad emission line centered at 594 nm with a shoulder at 589 nm is observed for the $^5D_0 \rightarrow ^7F_1$ transition whereas a resolved doublet (at 585 and 594 nm) with equal intensities is observed in monoclinic $Bi_{0.95}Eu_{0.05}PO_4$. The observed Eu^{3+} emission spectrum of monoclinic $BiPO_4$ is in agreement with the reported one.[6] It is known that the nanophosphors are much less efficient than the corresponding micron-sized phosphors.[39] The organic capping agents stabilize the nanoparticles by preventing the random aggregation of particles and limiting the particle growth. At the same time, these capping agents could create surface trap states that quench the PL emission of the nanophosphors. Alternate organic stabilizers are necessary to realize higher efficiencies with the rare earth based nanophosphors and optimization of particle size is also important in bridging the gap in PL emission efficiency between the nano and bulk phosphors.

4 Conclusions

Crystalline hexagonal $BiPO_4 \cdot xH_2O$ and $Bi_{0.95}Eu_{0.05}PO_4 \cdot xH_2O$ nanoparticles were synthesized by a polyol-mediated method. The water molecules present in the precursor, $Bi(NO_3)_3 \cdot 5H_2O$, favoured the formation of hydrated hexagonal $BiPO_4$. The hexagonal $Bi_{0.95}Eu_{0.05}PO_4 \cdot xH_2O$ was converted into monoclinic $Bi_{0.95}Eu_{0.05}PO_4$ with the loss of zeolitic lattice water molecules on heating at 600 °C. The morphological analysis by SEM and TEM showed the size of the primary nanoparticles is much less than 50 nm in the undoped and Eu^{3+}-doped hexagonal as well as monoclinic $BiPO_4$. The primary nanoparticles were stabilized by DEG to arrange themselves into cocoon-like microcrystallites. The DEG molecules could play an important role in retaining the particle size even after annealing at 600 °C at which the phase transition from hexagonal to monoclinic occurs. The crystal structural symmetry difference between the hexagonal and monoclinic $BiPO_4$ phase is evident from the spectral results of FT-IR, ^{31}P MAS-NMR and Eu^{3+} PL spectroscopies. The observed weak PL emission intensity of hexagonal $Bi_{0.95}Eu_{0.05}PO_4 \cdot xH_2O$ could be due to the presence of zeolitic water as well as surface bound residual DEG molecules which on removal led to the enhancement in the emission intensity along with the phase transition from hexagonal to monoclinic structure. The hexagonal $BiPO_4 \cdot xH_2O$ nanoparticles could find potential application in shape selective catalysis due to its open framework structure with hexagonal tunnels.

Acknowledgements

References

1 T. S. Chang, G. J. Li, C. H. Shin, Y. K. Lee and S. S. Yun, *Catal. Lett.*, 2000, **68**, 229–234.
2 V. G. Alekseev, I. P. Gorelov and M. V. Kornilov, *J. Anal. Chem.*, 2000, **55**, 1055–1057.
3 I-S. Cho, J. R. Kim, D. W. Kim and K. S. Hong, *J. Electroceram.*, 2006, **16**, 379–383.
4 Z. Holgye and R. Poliak, *J. Radioanal. Nucl. Chem.*, 1991, **153**, 267–272.
5 M. Roming and C. Feldmann, *J. Mater. Sci.*, 2009, **44**, 1412–1415.
6 M. Guan, J. Sun, F. Tao and Z. Xu, *Cryst. Growth Des.*, 2008, **8**, 2694–2697.
7 C. Pan and Y. Zhu, *Environ. Sci. Technol.*, 2010, **44**, 5570–5574.
8 C. Pan and Y. Zhu, *J. Mater. Chem.*, 2011, **21**, 4235–4241.
9 R. C. L. Mooney-Slater, *Z. Kristallogr.*, 1962, **117**, 371–385.
10 B. Romero, S. Bruque, M. A. G. Aranda and J. E. Iglesias, *Inorg. Chem.*, 1994, **33**, 1869–1874.
11 Y. F. Lin, H. W. Chang, S. Y. Lu and C. W. Liu, *J. Phys. Chem. C*, 2007, **111**, 18538–18544.
12 J. Geng, W. H. Hou, Y. N. Lv, J. J. Zhu and H. Y. Chen, *Inorg. Chem.*, 2005, **44**, 8503–8509.
13 M. Yang, N. K. Shrestha, R. Hahn and P. Schmuki, *Electrochem. Solid-State Lett.*, 2010, **13**, C5–C8.
14 C. Feldmann and H. O. Jungk, *Angew. Chem., Int. Ed.*, 2001, **40**, 359–362.
15 C. Feldmann, *Adv. Funct. Mater.*, 2003, **13**, 101–107.
16 G. Blasse and B. C. Grabmaier, *Luminescent Materials*, Springer-Verlag, Berlin, 1994.
17 G. Blasse and A. Bril, *J. Inorg. Nucl. Chem.*, 1967, **29**, 2231–2241.
18 B. Glorieux, M. Matecki, F. Fayon, J. P. Coutures, S. Palau, A. Douy and G. Peraudeau, *J. Nucl. Mater.*, 2004, **326**, 156–162.
19 R. D. Shannon and C. T. Prewitt, *Acta Crystallogr., Sect. B: Struct. Crystallogr. Cryst. Chem.*, 1969, **25**, 925–946.
20 A. R. West, *Solid State Chemistry and its Applications*, John Wiley and Sons, New York, 1984.
21 C. R. Patra, G. Alexandra, S. Patra, D. S. Jacob, A. Gedanken, A. Landau and Y. Gofer, *New J. Chem.*, 2005, **29**, 733–739.
22 M. T. Schatzmann, M. L. Mecartney and P. E. D. Morgan, *J. Mater. Chem.*, 2009, **19**, 5720–5722.
23 S. Lucas, E. Champion, D. Bernache-Assollant and G. Leroy, *J. Solid State Chem.*, 2004, **177**, 1312–1320.
24 F. Xue, H. B. Li, Y. C. Zhu, S. L. Xiong, X. W. Zhang, T. T. Wang, X. Liang and Y. Qian, *J. Solid State Chem.*, 2009, **182**, 1396–1400.
25 K. Nakamoto, *Infrared and Raman Spectra of Inorganic and Coordination Compounds, Part A*, John Wiley and Sons, New York, 1997.
26 S. Takeshita, J. Honda, T. Isobe, T. Sawayama and S. Nikura, *Cryst. Growth Des.*, 2010, **10**, 4494–4500.
27 A. Moguš-Milanković, A. Šantić, V. Ličina and D. E. Day, *J. Non-Cryst. Solids*, 2005, **351**, 3235–3245.
28 N. Kitamura, K. Ohno, K. Fukumi, J. Nakamura, T. Hidaka, T. Ikeda, H. Hashima, H. Kozuka and J. Nishii, *Jpn. J. Appl. Phys.*, 2010, **49**, 082601–1-082601-4.
29 W. Kemp, *Organic Spectroscopy*, 3rd Ed., The Macmillan Press Ltd., Hong Kong, 1994.
30 R. S. Macomber, *A. Complete Introduction to Modern NMR Spectroscopy*, John Wiley & Sons, Inc., New York, 1998.
31 G. Blasse, *J. Solid State Chem.*, 1972, **4**, 52–54.
32 L. Li, Y. Su and G. Li, *J. Mater. Chem.*, 2010, **20**, 459–465.
33 S. W. Buckner, R. L. Konold and P. A. Jelliss, *Chem. Phys. Lett.*, 2004, **394**, 400–404.
34 A. K. Gulnar, V. Sudarsan, R. K. Vatsa, R. C. Hubli, U. K. Gautam, A. Vinu and A. K. Tyagi, *Cryst. Growth Des.*, 2009, **9**, 2451–2456.
35 G. Blasse, A. Bril and W. C. Nieuwpoort, *J. Phys. Chem. Solids*, 1966, **27**, 1587–1592.
36 N. Lakshminarasimhan and U. V. Varadaraju, *J. Solid State Chem.*, 2004, **177**, 3536–3544.
37 N. Lakshminarasimhan and U. V. Varadaraju, *J. Solid State Chem.*, 2005, **178**, 3284–3292.
38 C. Zollfrank, H. Scheel, S. Brungs and P. Greil, *Cryst. Growth Des.*, 2008, **8**, 766–770.
39 J. M. Phillips, M. E. Coltrin, M. H. Crawford, A. J. Fischer, M. R. Krames, R. Mueller-Mach, G. O. Mueller, Y. Ohno, L. E. S. Rohwer, J. A. Simmons and J. Y. Tsao, *Laser Photonics Rev.*, 2007, **1**, 307–333.
40 K. Momma and F. Izumi, *J. Appl. Crystallogr.*, 2008, **41**, 653–658.